Article:
Mei, Shangming, Hu, Yihua and Nasr Esfahani, Mohammad (2026) Adaptive Optimization of Non-Uniform Phased Array Speakers Using Particle Swarm Optimization for Enhanced Directivity Control. Modelling. 20. ISSN: 2673-3951

https://doi.org/10.3390/modelling7010020

modelling

MDPI

Article

Adaptive Optimization of Non-Uniform Phased Array Speakers Using Particle Swarm Optimization for Enhanced Directivity Control

Shangming Mei [1], Yihua Hu [2] and Mohammad Nasr Esfahani [1,*]

[1] School of Physics, Engineering and Technology, University of York, York YO10 5DD, UK; sm2747@york.ac.uk
[2] Department of Engineering, King's College London, London WC2R 2LS, UK; yihua.hu@kcl.ac.uk
* Correspondence: mohammad.nasresfahani@york.ac.uk

Abstract

Phased array speakers are often designed with uniform element spacing, which limits beam steering capability and sidelobe control under practical aperture and hardware constraints. This study presents an optimization-driven modelling framework for parametric array loudspeakers (PALs) that systematically links array layout synthesis with high-fidelity directivity prediction, by combining a frequency-domain convolution model with a finite element method (FEM) pipeline. We formulate array layout synthesis as a constrained optimization problem and employ particle swarm optimization (PSO) to determine non-uniform element positions that suppress sidelobes while preserving mainlobe integrity across steering angles. By integrating linear acoustic field simulation with far-field directivity prediction, the framework serves as a computationally efficient surrogate model suitable for iterative design under non-ideal spacing conditions. Simulation results and laboratory measurements demonstrate that the optimized non-uniform arrays achieve consistently lower sidelobe levels and more concentrated mainlobes than conventional uniform configurations. These results validate the proposed framework as a practical and reproducible solution for steering-capable PAL design when the conventional $\lambda/2$ spacing constraint cannot be satisfied and establish a foundation for subsequent robustness and sensitivity analyses.

Keywords: parametric array loudspeaker; phased array; particle swarm optimization; sidelobe suppression; beam steering; finite element method

Academic Editor: Rostand B. Tayong

Received: 7 November 2025
Revised: 8 January 2026
Accepted: 13 January 2026
Published: 15 January 2026

1. Introduction

PALs serve various applications that require precise sound field control. They are characterized by high directivity and by exploiting nonlinear propagation in air to generate audible sound through self-demodulation of ultrasonic carriers [1–4]. A distinctive feature of these devices is their ability to project sound in a specific direction with limited diffraction, resulting in a narrow beam at ultrasonic frequencies [5]. This principle underpins their utility in directional sound systems that reduce noise while providing a clear auditory signal to a targeted area [6]. These devices, leveraging ultrasonic wave functions as carriers of audible frequencies, are especially useful in environments where ambient noise reduction is crucial, such as public address systems, home theatres, and transportation vehicles like aircraft and buses [7,8].

Adaptive parametric array loudspeakers extend conventional designs by using phased-array techniques to steer audio beams electronically, without mechanical rotation. This

technology has been explored for applications such as active noise control and directional sound reproduction. An adaptive system typically uses a linear array of ultrasonic transducers, in which beam direction is controlled by phase delays across elements [9,10].

To avoid grating lobes, which degrade directivity, element spacing is usually kept at half the wavelength or less. Exceeding this spacing threshold leads to spatial aliasing, where grating lobes interfere with the main lobe. Although reducing the spacing can suppress grating lobes, meeting the half-wavelength criterion is often difficult due to transducer size constraints [11–13].

To address the challenges posed by sidelobe interference and spatial aliasing in PALs, this study proposes an optimal sparse array technique to improve adaptive PAL design, particularly in scenarios where the Nyquist criterion cannot be met. In recent years, increasing attention has been paid to beamforming and array configuration strategies for PALs, particularly under practical constraints such as limited aperture size and non-ideal element spacing. Various approaches have been investigated, including analytical directivity modelling, numerical simulation based on FEMs, and array synthesis techniques aimed at suppressing sidelobes and grating lobes. More recent studies have also explored non-paraxial modelling, steerable array configurations, and non-uniform or disordered layouts to improve directivity performance beyond the limitations of conventional uniform arrays [4,14,15].

Despite these advances, the optimization of non-uniform PAL layouts remains challenging due to the highly nonlinear relationship between array geometry and acoustic directivity, especially when experimental uncertainties and hardware constraints are considered. This motivates the need for efficient optimization frameworks that can systematically explore the design space while remaining compatible with high-fidelity numerical modelling. By employing non-uniform array configurations as shown in Figure 1, this approach helps smooth the lobe structure and mitigate high sidelobe occurrences, thereby enhancing overall beamforming accuracy and signal-to-noise ratio. However, optimizing non-uniform arrays introduces greater complexity, requiring advanced computational techniques for precise element positioning.

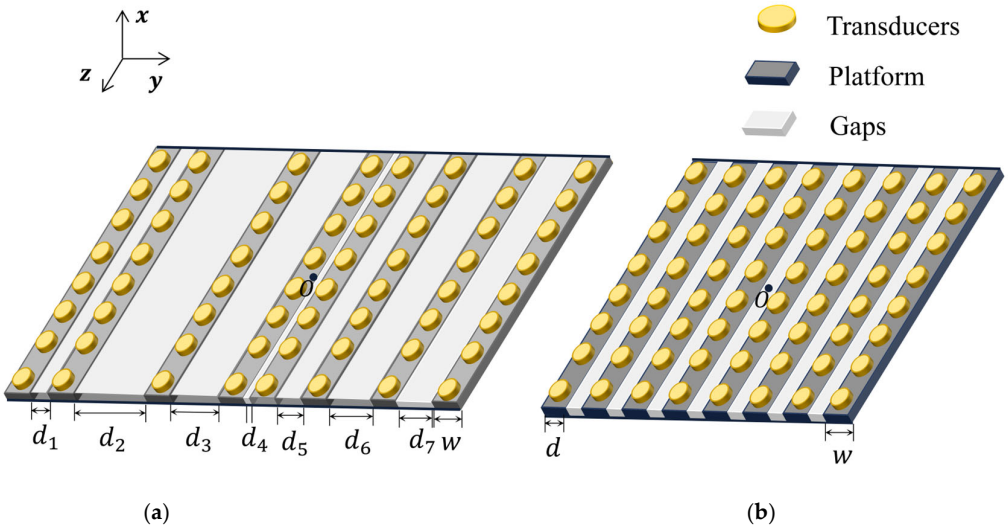

Figure 1. Schematic of the parametric array loudspeaker system and the ultrasonic demodulation process in air: (**a**) sparse array and (**b**) uniform array.

To achieve this, we employ particle swarm optimization to determine the transducer positions offline, optimizing directivity across multiple steering angles. Unlike approaches that assume fixed or uniformly spaced arrays, the proposed method optimizes element positions under practical spacing constraints to achieve improved sidelobe suppression and

directional control. By dynamically optimizing the element positions, PSO enables a more flexible and efficient solution. The key contribution of this work lies in formulating the non-uniform PAL layout design as a constrained optimization problem that explicitly accounts for steering-angle dependency and practical spacing limitations, rather than assuming idealized or fixed array geometries.

Additionally, to accurately model the acoustic field and assess the impact of different array configurations, we employ the FEM, which enables high-fidelity simulation of acoustic wave propagation. While traditional analytical models such as Westervelt and Khokhlov–Zabolotskaya–Kuznetsov (KZK) equations offer useful approximations, they are often constrained by simplifying assumptions like paraxial approximations or limited boundary conditions. In contrast, FEM offers greater flexibility for handling complex geometries, boundary conditions, and near-field effects, making it well-suited for modelling the acoustic behaviour of PALs. By capturing wave interactions more accurately, FEM supports a realistic understanding of diffraction, beamforming, and directivity patterns in practical scenarios [16–18].

Different from existing PAL optimization studies that rely solely on analytical formulations or fixed-spacing assumptions, the proposed approach integrates PSO-based array synthesis with FEM-based directivity evaluation, allowing optimization decisions to be guided by high-fidelity numerical modelling under realistic constraints. In this study, numerically optimized non-uniform array configurations are first identified across different steering angles and subsequently selected as reference designs for experimental validation, ensuring a consistent and systematic numerical-to-experimental workflow.

The following sections present the theoretical background of PALs, including sound pressure modelling, attenuation, and nonlinear directivity. We then introduce the optimization algorithm used in this study and describe the experimental setup, measurement methods, and data analysis. Finally, we compare simulation and experimental results to evaluate performance and conclude with insights into the practical implications and limitations of the proposed approach.

2. Materials and Methods

This section describes the modelling and evaluation procedures used in this study. We first introduce the key acoustic quantities required for far-field prediction, including sound pressure, atmospheric attenuation, sound pressure level, and directivity. We then present the nonlinear (Westervelt-based) formulation and the convolution-based directivity model adopted for efficient far-field estimation. Finally, we detail the optimization problem formulation and the algorithmic settings used to synthesize sparse array layouts.

2.1. Sound Pressure Calculation

In this work, we utilize the Pressure Acoustics, Frequency Domain interface from the Pressure Acoustics branch for modelling acoustic wave propagation in fluids. To optimize computational resources, our model is constructed in two dimensions, incorporating a line sound source which produces a cylindrical sound wave. The physics interface solves the Helmholtz equation in the frequency domain for specified frequencies or performs an eigenfrequency or mode analysis study. This interface efficiently computes pressure variations by solving the Helmholtz equation in the frequency domain and is particularly suited for frequency-domain simulations involving harmonic pressure field variations.

The primary variable, the sound pressure p_t, encapsulates the acoustic perturbations relative to the ambient pressure. For 2D models, the default out-of-plane wave number is set to $k_z = 0$ rad/m, indicating no variation along the z-axis, thereby simplifying the pressure expression in our simulations.

Figure 2 compares the two-dimensional and three-dimensional configurations used in this study. The primary ultrasonic field exhibits a highly directional main lobe along the beam axis and sidelobes that correspond to undesired energy leakage. In practical applications, sidelobe suppression is critical because strong sidelobes may introduce audible interference outside the intended listening region.

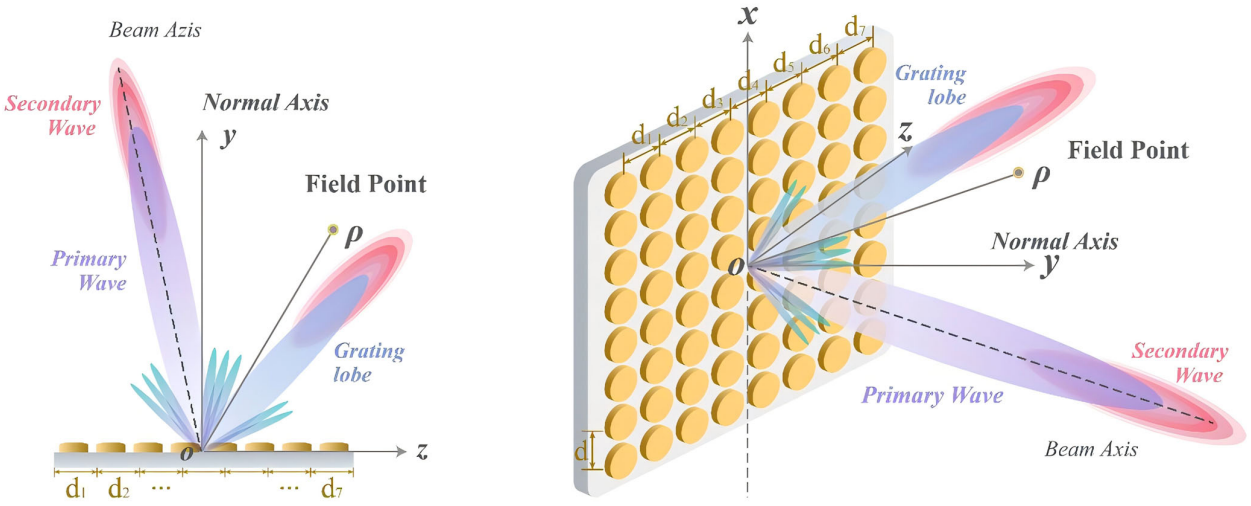

(**a**) (**b**)

Figure 2. The linear acoustic phased array and corresponding sound field: (**a**) an 8-element configuration in the two-dimensional model; (**b**) a 64-element configuration in the three-dimensional model. Both cases are illustrated at a representative steering angle.

In the simulation, a two-dimensional linear sound source is created by reducing the dimensionality of the three-dimensional model. This is achieved by using the line source on axis node to introduce a line source along the axis of symmetry in 2D components. This line source represents a radially vibrating cylinder in the limit as its radius approaches zero. The sound pressure value of any point in the calculation space can be obtained by solving the partial differential Equation (1) using the FEM.

$$\nabla \cdot \left(-\frac{1}{\rho_c}(\nabla p_t - \mathbf{q}_d) \right) - \frac{k_{eq}^2 p_t}{\rho_c} = \frac{4\pi}{\rho_c} S\delta(z - z_0)dz \tag{1}$$

$$k_{eq}^2 = \left(\frac{\omega}{c_c} - i\alpha \right)^2 - k_z^2 \tag{2}$$

where p_t represents the total acoustic pressure, ρ is the fluid density, c is the speed of sound, $\mathbf{q}_d$ denotes the dipole domain source, complex density $\rho_c = \frac{\rho c^2}{c_c^2}$, complex speed of sound as $c_c = \omega/k - i\alpha$. In this context, $\delta(z - z_0)$ is the 2D delta function that introduces the source at the axis of symmetry, where $z = z_0$ and $r = 0$, while dz represents the line element along the z axis (SI unit: m). The monopole amplitude S (SI unit: N/m^2) is determined by the type of source selected and is analogous to the 3D case for a line source. To include an edge source at $r = r_0$, define it using the volume flow rate per unit length Q_S and the phase φ of the source. The flow edge source then establishes the monopole amplitude as (3):

$$S = e^{i\phi} \frac{i\omega\rho_c}{4\pi} Q_S \tag{3}$$

A flow edge source with strength Q_S represents an area flow emitted from the source, modeled as a very thin cylinder with a pulsating surface. Specify Q_S (SI unit: m^2/s), the

volume flow rate per unit length from the source, as the amplitude for the source strength in the field.

2.2. Attenuation Coefficient

The attenuation coefficient of sound in air is crucial in determining how sound energy diminishes during propagation, depending on factors like frequency, temperature, pressure, and humidity. It directly influences sound field predictions and helps refine applications such as ultrasonic and acoustic wave simulations, which can be defined as

$$\alpha = f^2\Big[1.84\times10^{-11}\,\frac{p_r}{p_a}\left(\frac{T}{T_0}\right)^{\frac{1}{2}} + \left(\frac{T}{T_0}\right)^{-\frac{5}{2}}\left(\frac{0.01275e^{-\frac{2239.1}{T}}}{f_{r,o}+\frac{f^2}{f_{r,o}}}+\frac{0.1068e^{-\frac{3352.0}{T}}}{f_{r,N}+\frac{f^2}{f_{r,N}}}\right)\Big]\left(\frac{\mathrm{NP}}{\mathrm{m}}\right) \tag{4}$$

where p_a is the air pressure in the propagation environment, $p_r = 101.325$ kPa is baseline ambient air pressure, $\mathrm{T}_0 = 293.15$ K is the standard air temperature $(20\ ^\circ\mathrm{C})$, $f_{r,o}$ and $f_{r,N}$ are the oxygen relaxation frequency and nitrogen relaxation frequency, respectively [19,20], expressed as:

$$f_{r,O} = \frac{p_a}{p_r}\left(24 + 4.04\times10^4 h\frac{0.02+h}{0.391+h}\right) \tag{5}$$

$$f_{r,N} = \frac{p_a}{p_r}\left(\frac{T}{T_0}\right)^{-\frac{1}{2}}\left(9+280h_r{}^{-4.17[(\frac{T}{T_0}{}^{-\frac{1}{3}}-1)]}\right) \tag{6}$$

In the function (6), T is the temperature and $T_0 = 293.15$ K, absolute humidity h can be presented by the relative humidity $\mathrm{h_r}$, and the saturated water vapor pressure p_{sat}, by the following equation:

$$h = h_r\frac{p_{\mathrm{sat}}}{p_r}\frac{p_a}{p_r} \tag{7}$$

p_{sat} is given by the modified Tense formula as:

$$p_{\mathrm{sat}} = 0.6112\times\exp\left(\frac{17.67\mathrm{t}}{t+243.5}\right) \tag{8}$$

2.3. Sound Pressure Level and Directivity

Sound Pressure Level (SPL) is a fundamental concept in acoustics used to describe the intensity of sound pressure relative to a reference pressure [21]. It is expressed in decibels (dB) and is calculated using the formula which is calculated by the sound pressure p_{t}:

$$L(\phi) = 20\log_{10}\left(\frac{p_{\mathrm{t}}(\phi)}{P_{\mathrm{ref}}}\right) \tag{9}$$

where P_{ref} is the reference sound pressure is 20 µPa$\left(20\cdot10^{-6}\ \mathrm{Pa}\right)$. The directivity pattern based on SPL is calculated as the relative difference between the measured SPL at a given angle ϕ and the SPL at a reference angle (typically the direction of maximum response, e.g., $\phi = 0^\circ$). It is given by

$$D_{\mathrm{SPL}}(\phi) = L(\phi) - L(\phi_{\mathrm{ref}}) \tag{10}$$

2.4. Nonlinear Acoustics (Westervelt) Directivity

The Westervelt Equation in (11) provides a foundational framework for predicting the directivity of PALs, with directional characteristics influenced by the ultrasonic attenuation coefficient and source frequency [22,23]. Shi and Kajikawa (2015) introduced a convolution model that combines Westervelt directivity with ultrasonic directivity, significantly enhancing computational efficiency and far-field directivity prediction [24]. This approach

is particularly effective for modelling the main lobe, though additional models may be needed for accurate sidelobe estimation [25].

Recent advancements have refined the convolution model, which remains advantageous due to its speed and accuracy in far-field cases [24,25]. The model considers a circular PAL on an infinitely reflective surface, where ultrasound beams interact through second-order nonlinearity to generate an audible secondary wave [19]. Both 2D and 3D representations of this setup define a Cartesian coordinate system centred at the loudspeaker array, with the z-axis aligned with the sound radiation direction [21]. In the following, the Westervelt equation is used to derive the far-field solution for phase loudspeaker arrays, leveraging the convolution model for accurate far-field predictions.

$$\nabla^2 p - \frac{1}{c^2}\frac{\partial^2 p}{\partial t^2} = -\frac{\delta}{c^4}\frac{\partial^3 p}{\partial t^3} - \frac{\beta}{\rho_0 c^4}\frac{\partial^2 p^2}{\partial t^2} \tag{11}$$

where δ is the diffusivity of sound and β is the coefficient of nonlinearity, where ρ_0 represent the ambient air density, p denotes the sound pressure, which is linked to the sound attenuation coefficient α.

The Westervelt equation is employed to accurately model the behaviour of PAL under second-order nonlinearities in the far field. This equation uses a stepwise approach to simulate the quasi-linear solution of audio sound, which is treated as emission from an infinite virtual source with a specified sound pressure [19]. Consequently, the convolution directional model equation for the PAL sound can be derived as follows [24]:

$$\begin{array}{c} D_a(\varphi) = (D_1 * D_2 \times D_w)(\varphi) \\ = \int_0^{2\pi} D_1^*(\varphi_v) D_2(\varphi_v) D_w(\varphi - \varphi_v) d\varphi_v \end{array} \tag{12}$$

We define an integral called Westervelt's directivity as [4]:

$$\begin{array}{c} D_w(\varphi) \equiv (\alpha_1 + \alpha_2) \int_0^{+\infty} e^{i[k_2 - k_1 * - k_a cos(\varphi - \varphi_v)]\rho_v} \, \mathrm{d}\rho_v \\ = \dfrac{1}{1 - ik_a \dfrac{\alpha_1 + \alpha_2}{2}^{-1} sin^2\left(\dfrac{\varphi - \varphi_v}{2}\right)} \end{array} \tag{13}$$

where $k = 2\pi/z$, α_1 and α_2 are weighting factors; In the two-dimensional piston model, the velocity distribution of the ultrasound is uniform $u_j(\rho_s) = 1$, $\rho_s \leq r$, where the directivity of the corresponding ultrasound is $D_j(\varphi)$ which was derived from an acoustic model generated by (10). Because the calculation of the distribution of the second harmonic is too large and huge errors will be generated by directly using the FEM to solve it, this paper uses the FEM to synthesize product directivity ($D_1 * D_2$) and puts product directivity into (12) to obtain the directivity of the second harmonic.

Grating lobes occur when the inter-element spacing exceeds one wavelength. In this regime, the grating-lobe amplitude can become comparable to the main-lobe amplitude. For a linear phased array, the phase shift across the array as a function of beam angle is given by

$$\Delta\Phi = \frac{2\pi d sin\theta}{\lambda} \tag{14}$$

Then, the steering angle can be calculated as a function of the phase shift:

$$\theta = arcsin\left(\frac{\Delta\Phi}{2\pi} \times \frac{\lambda}{d}\right) \tag{15}$$

where $\Delta\Phi$ is the phase shift between adjacent elements; d is the inter-element spacing; the acoustic wavelength $\lambda = c/f$. In general, the inter-element spacing should be smaller

than half the wavelength (≈4 mm at 40 kHz in air). Determining the optimal sparse array configuration is challenging due to the complex relationship between array structure and beamforming performance. The optimization method used in this study is described in the following section.

2.5. Optimization Method

Extensive research has been conducted on phased array position optimization, with techniques such as Teaching Learning-Based Optimization (TLBO) [26], Quantum Particle Swarm Optimization (QPSO) [27], Symbiotic Organisms Search (SOS) [28], and machine-learning-based genetic algorithms [29] being applied to improve element placement. These methods aim to generate specific beam patterns (e.g., pencil beams, flat-top beams [30]) while effectively reducing sidelobe levels. As phased array beamforming is a nonlinear, multivariable optimization problem, these studies offer valuable strategies that can also be extended to PAL design.

In high-dimensional optimization tasks, PSO, Simulated Annealing (SA), and Genetic Algorithm (GA) are commonly used. PSO is known for its fast convergence and population-based search, making it suitable for large-scale problems, though it requires careful parameter tuning to avoid premature convergence [31–33]. SA offers strong global search capability by accepting suboptimal solutions early on, but its single-solution updates and dependence on temperature control can reduce efficiency [34,35]. GA promotes solution diversity, helping to avoid local optima, but may suffer from slow convergence and complex tuning, especially in high-dimensional cases [36].

The computational efficiency of the proposed PSO-based optimization framework was further evaluated through a comparative study involving PSO, GA, and SA under identical function evaluation (FE) budgets. All algorithms were applied to the same optimization problem: maximizing the difference between the main lobe sound pressure level and the maximum sidelobe level of an 8-element PAL steered toward a predefined angle.

To ensure fairness in computational cost, all algorithms were allocated the same FE budget, defined as the total number of sound field calculation program (COMSOL Multiphysics 6.1) calls. Specifically, a maximum of 100 FEs per run was used for each algorithm. Each algorithm was independently executed 30 times, starting from the same randomly generated initial configurations. For PSO and GA, identical initial populations were used, while SA was initialized from the same starting solution in each run. All random seeds were controlled to guarantee reproducibility.

An eight-element two-dimensional PAL array was considered in this study. The optimization variables were the seven inter-element gaps between adjacent ultrasonic transducers, while the element length was fixed to 1 cm. The steering angle was fixed to $\psi = 75^{\circ}$, and all optimization algorithms aimed to maximize the difference between the main lobe sound pressure level and the highest sidelobe level (which is defined as Δ) in the far field. The far-field sound pressure distribution was sampled on a two-dimensional grid, and the directivity pattern was obtained by angular averaging. The objective function is given in function (16).

Figure 3 presents the mean convergence curves over 30 independent runs, where the shaded regions indicate one standard deviation. Particle swarm optimization and genetic algorithms achieve rapid improvement during the initial stage, exceeding 1 dB mean main-to-sidelobe improvement within the first 10 evaluations, whereas simulated annealing shows slower initial progress. With increasing FE count, particle swarm optimization consistently attains the highest mean Δ, followed by genetic algorithms, while simulated annealing converges to a lower level. After 100 evaluations, the mean Δ achieved by particle swarm optimization is approximately 0.3–0.6 dB higher than that of the other two methods.

Genetic algorithms exhibit the smallest variance across runs, indicating better repeatability, whereas simulated annealing shows larger dispersion, suggesting higher sensitivity to the initial condition and stochastic perturbations. Considering both solution quality and computational efficiency under limited evaluation budgets, particle swarm optimization is adopted for the subsequent array optimization in this work.

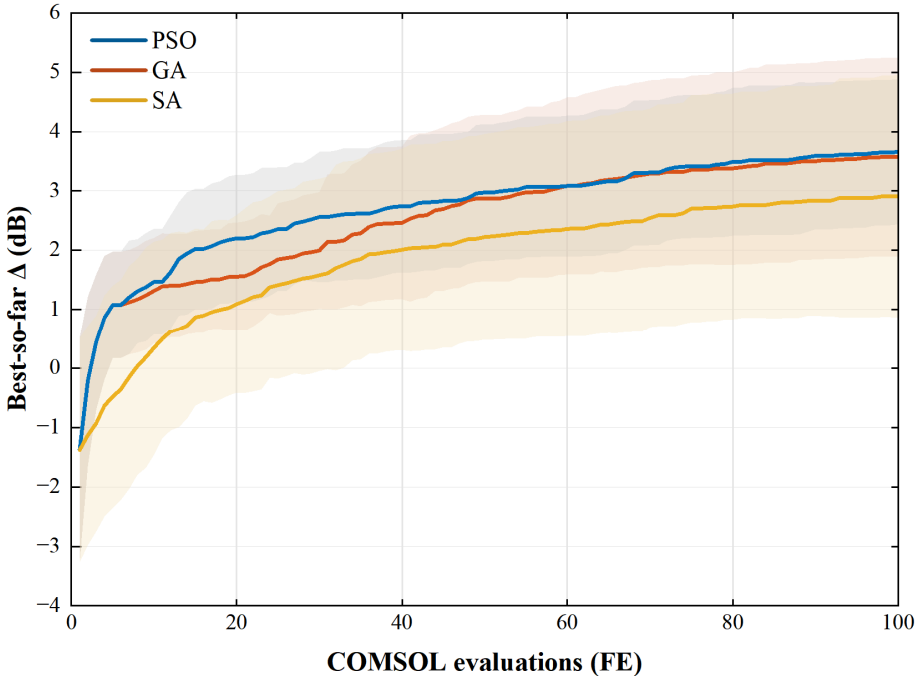

Figure 3. Graph illustrating the mean convergence curves of PSO, GA, and SA over 30 independent runs.

2.6. Cost Function and Algorithm

In this study, the cost function is defined as the maximum difference between the sound pressure of the main lobe and the highest sidelobe, with a constraint added to maintain sufficient main lobe strength. To keep the overall aperture within practical hardware and measurement constraints, the initial sound pressure level is fixed at 1, while transducer spacing varies from 0 cm to 1.3 cm. The upper bound ensures that the overall array size remains within twice the wavelength, preventing overly large configurations. The sampling approach and cost evaluation follow previously established protocols, with all arrays centred at the origin.

To ensure that the size of the main lobe is not smaller than a fixed value, another restriction needs to be added, where $\mathrm{SPL}_{\mathrm{Main}}$ is the sound pressure level of the main lobe:

$$C(\mathbf{x}) = \begin{cases} J(\psi) = \max(L_{\mathrm{Main}}(\psi) - L_{\mathrm{Side}}(\psi)) & \text{if } L_{\mathrm{Main}}(\psi) > 80 \text{ dB} \\ \text{large penalty} & \text{otherwise} \end{cases} \tag{16}$$

where ψ is the Optimal Steering angle, Beam width of the main lobe $\Delta\varphi > 0$ is set to cover the main lobe, $L_{\mathrm{Main}}(\psi)$ is the peak value of the main lobe at ψ. the element x-axis position vector $\mathbf{x} = [x_1, x_2, \ldots, x_N]^{\mathrm{T}}$, and the superscript "T" denotes a matrix transpose. The peak sidelobe level (PSL) is employed in this study as a key metric to evaluate the performance of the array configuration. The optimization task is formulated as a global minimization problem, where the objective function is minimized by adjusting the transducer position **x**. The detailed optimization procedure is outlined in Algorithm 1.

Algorithm 1 PSO-Driven FEM Optimization

START
Initialize particle population $\mathbf{x} = [x_1, x_2, \ldots, x_N]^T$
Set SPL $= 1$, spacing bounds: $[0, 1.3\ \text{cm}]$
FOR each iteration:
FOR each particle $\mathbf{x_i}$ DO
Transfer $\mathbf{x}_i$ to COMSOL FEM model
Run FEM: compute pressure field $p(\mathbf{r})$
Convert to SPL: $L = 20\log_{10}\left(\frac{p_t}{P_{\text{ref}}}\right)$, $P_{\text{ref}} = 20\ \mu\text{Pa}$
Extract directivity pattern $L(\phi)$
Find main lobe: $L_{\text{Main}}\ (\psi) = \max_{\phi \in \Delta\phi} L(\phi)$
Find 3 highest sidelobes: $\left\{ L_{\text{Side}}^{(k)} \right\}_{k=1}^{3}$
Evaluate cost: $J(\mathbf{x}_i) = \max L_{\text{Side}}^{(k)} - L_{\text{Main}}\ (\psi)$
If $L_{\text{Main}}\ (\psi) < 80$ dB, apply penalty to $J(\mathbf{x}_i)$
ENDFOR
Update particles:
$\mathbf{v}_i(t+1) = \omega \mathbf{v}_i(t) + c_1 r_1 (\mathbf{p}_i - \mathbf{x}_i) + c_2 r_2 (\mathbf{g} - \mathbf{x}_i)$
$\mathbf{x}_i(t+1) = \mathbf{x}_i(t) + \mathbf{v}_i(t+1)$
ENDFOR
Return $\mathbf{x}^*$, optimal directivity pattern

COMSOL Multiphysics 6.1 is used to solve the ultrasonic pressure field using the finite element method, while the optimization loop is implemented in MATLAB 2022b. The overall co-simulation workflow is illustrated in Figure 4. For each candidate array configuration, COMSOL returns the pressure field, which is converted to sound pressure level and sampled along a far-field observation arc to obtain the directivity pattern. The main-lobe peak at the target steering angle and the peak sidelobe level outside a predefined main-lobe window are extracted to evaluate the cost function. MATLAB then updates the array configuration according to particle swarm optimization and passes the updated parameters back to COMSOL for the next evaluation.

The simulations are conducted in a rectangular computational domain designed to approximate the experimental environment. Absorbing (radiation) boundary conditions are applied to suppress artificial reflections from the domain boundaries. The acoustic source is modelled as an 8-element array located along the bottom boundary. In the two-dimensional model, each element is represented by an equivalent line segment corresponding to a circular transducer of 10 mm diameter in the three-dimensional setup. The element positions are treated as design variables and are iteratively updated by the MATLAB optimizer.

The propagation medium is air at standard atmospheric pressure, with 50% relative humidity and a temperature of 13 °C. The finite element simulations consider linear acoustics for the ultrasonic field; the audible demodulation process is not directly solved in the finite element model and is instead addressed through the analytical/convolution-based formulation described earlier. The optimization outcomes and convergence characteristics are reported in Section 4.

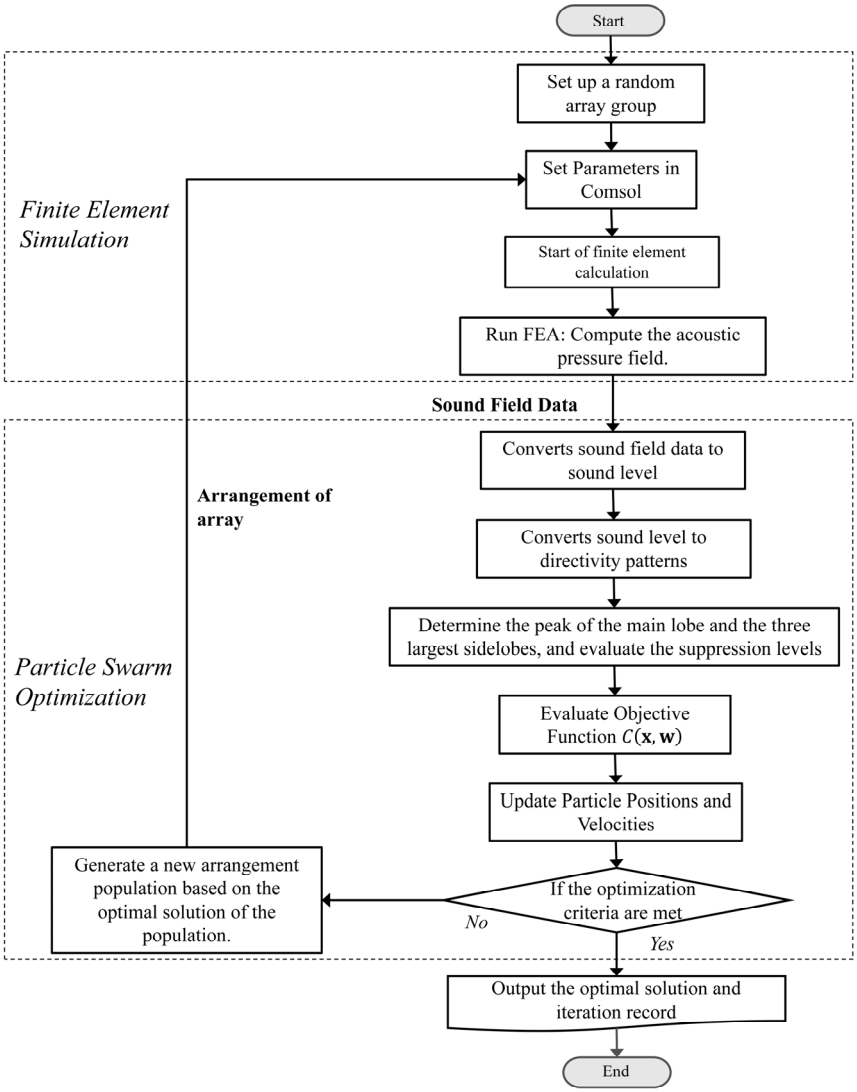

Figure 4. Integration Diagram of COMSOL and MATLAB for Co-Simulation in Speaker Array Optimization.

3. Experimental Setup and Measurements

3.1. Measurement Setup

Based on the numerical optimization results in Section 4, representative non-uniform array configurations at steering angles of 60°, 65°, 70°, and 75° were selected for experimental validation. In addition, a Monte Carlo analysis was conducted for these representative cases to assess the sensitivity and robustness of the proposed method under practical uncertainties.

All measurements were conducted in a quiet and controlled anechoic chamber to suppress background noise and minimise acoustic reflections. The array was driven by ultrasonic carrier signals at 40 kHz and 42 kHz generated by an Arduino-based controller. Sound pressure levels were captured using a calibrated measurement microphone, together with a signal generator, an audio interface, and signal analysis software. The microphone was positioned 2 m from the array, and the directivity patterns were obtained by sampling the measurement arc at 2.5° angular intervals. The key parameters of the experimental setup are summarized in Table 1. The recorded signals were subsequently processed to extract the directivity responses of the optimized configurations.

Table 1. Key parameters of the experimental setup for measuring array directivity.

Parameter	Value
Distance between speaker and microphone	2 m
Temperature T	13 °C
Piezoelectric Transducer Diameter	1 cm
Frequency f	40,000 Hz, 42,000 Hz
Optimal Steering angle ψ	60°, 65°, 70°, 75°

The Arduino generates eight digital drive signals as binary pulse trains. These signals are output cyclically, where phase control is achieved by shifting the waveform timing and amplitude control is implemented via duty-cycle adjustment. Although square-wave excitation is used for simplicity in the digital design, the transducer resonance produces a near-sinusoidal acoustic output.

Measurements were conducted in an anechoic chamber, as shown in Figure 5a. The chamber measures 3.0 m × 3.5 m and is located in a separate building to provide acoustic isolation. Foam wedges cover all surfaces to suppress reflections, and a suspended mesh floor allows access without compromising measurement quality. During testing, the array was mounted vertically on the rotary table and centred on the rotation axis. The microphone was placed 2 m from the array. The array was powered at an output voltage of 12 V.

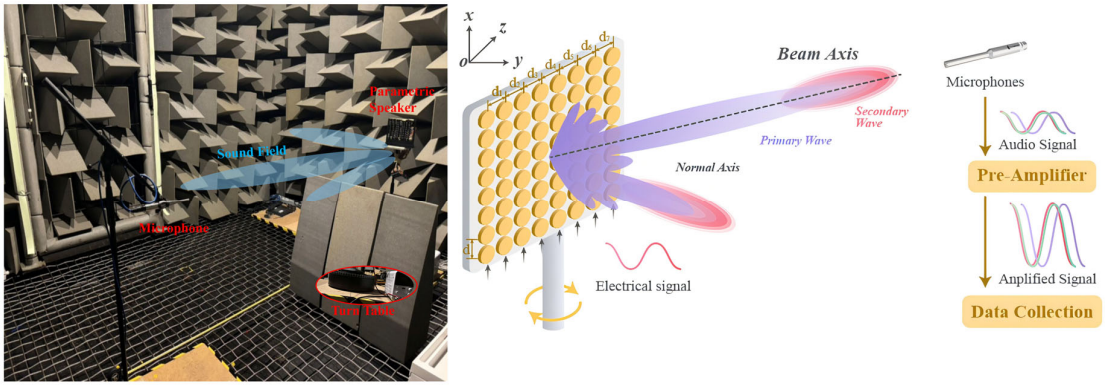

(**a**) (**b**)

Figure 5. (**a**) Anechoic chamber setup with a 2 m distance between the microphone and PAL; ambient temperature maintained at 13 °C. (**b**) Transducer array setup: signals from the microcontroller are amplified and sent to each transducer; received acoustic signals are captured and pre-amplified for analysis.

An Earthworks M30 microphone(Earthworks Audio, Milford, NH, USA) was used to acquire acoustic data. The microphone supports measurements up to 95 kHz. Key specifications include a self-noise level of 20 dBA, a sensitivity of −29 dBV/Pa, and a 24–48 V phantom power supply (10 mA). Although the nominally flat response is specified below 30 kHz, the microphone was used in this study to capture ultrasonic signals at 40–42 kHz with consistent measurement settings across all cases.

3.2. Measurement Procedure

As shown in Figure 5b, the measurement procedure was carried out based on the experimental setup described in Section 3.1. First, the array was mounted on the rotary table and aligned with the measurement microphone along the main radiation axis at a fixed distance of 2 m. The driving signals were generated by the Arduino-based control system, where the phase and amplitude of each channel were configured according to the predefined array configuration and steering angle.

For each test case, the array was driven with ultrasonic carriers at 40 kHz and 42 kHz. The steering angle was set by applying the corresponding phase delays to each channel. The sound pressure level was recorded by the measurement microphone while the rotary table was rotated in angular steps of 2.5°, covering the entire measurement arc.

At each angular position, the acoustic signal was acquired and processed using the audio analysis software to extract the SPL. The resulting angular sound pressure level data were then used to construct the directivity patterns for both uniform and optimized configurations. This procedure was repeated for all selected steering angles and array configurations to ensure consistent comparison between simulation and experimental results.

4. Results and Discussion

This section presents the optimization simulations, experiments, and analysis results, with a focus on the performance improvements achieved using the PSO algorithm. The analysis includes comparisons of sound pressure levels, directivity patterns, and the impact of different transducer arrangements.

4.1. Optimization Results and Convergence Behaviour

Based on the optimization procedure described in Section 2, this section analyses the convergence behaviour and performance of the optimized array configurations. The optimized layouts were obtained for different steering angles by systematically adjusting the steering direction and identifying the corresponding transducer arrangement that best improves the sound pressure distribution and suppresses sidelobes. The simulation methodology and array topology are described in the Simulation section above. As described in Section 2, random perturbations were applied to stagnating particles to reduce the risk of premature convergence to local minima. This mechanism improved exploration and led to consistent optimization behaviour across repeated runs.

The optimization results in Figure 6 and Table 2 show a clear dependence on the steering angle ψ. Overall, the optimized arrays achieve larger main-lobe–to–sidelobe separation at higher steering angles, indicating that non-uniform spacing can mitigate grating-lobe effects within the considered steering range. Nevertheless, sparse layouts remain subject to practical limitations, and excessive steering may still lead to degraded sidelobe performance.

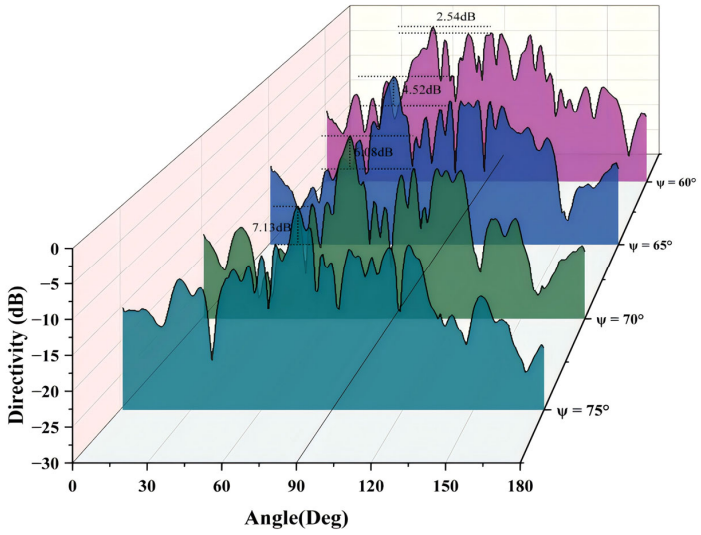

Figure 6. Directivity patterns of an optimized array with 8 elements ($N = 8$), each with a width of 1 cm, operating at an ultrasound frequency of 40 kHz (f = 40 kHz). The patterns are shown for optimal angles ψ of 60°, 65°, 70° and 75°. The colour variations represent the results of three independent simulations conducted under the same conditions.

Table 2. Array optimization results at different steering angles ψ and comparison with the results of the linear array.

ψ (°)	Optimized Array Δ (dB)	Uniform Array Δ (dB)
60	2.5486	−3.1203
65	4.5273	−0.7920
70	6.0791	1.2819
75	7.1327	5.2665

We performed multiple runs to ensure the robustness of the optimization results. The final optimized array configurations for each steering angle are shown in Figure 7.

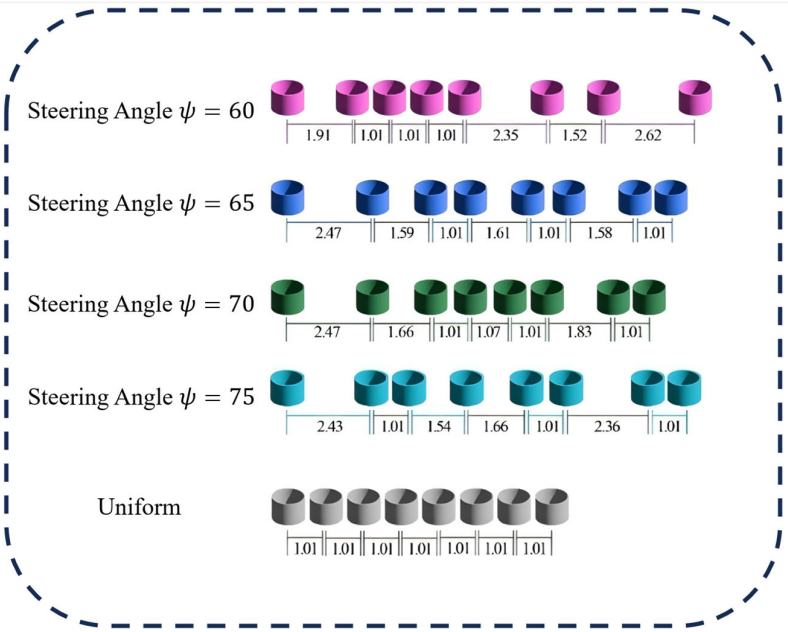

Figure 7. The best array configurations obtained through optimization for different optimal angle ψ. The array consists of 8 elements, each with a base length of 1 cm, and operates at an average ultrasound frequency of 40 kHz (f = 40 kHz).

Table 2 compares the main-lobe–sidelobe difference (Δ, in dB) between the optimized arrays and the uniform array for steering angles $\psi = 60°$, 65°, 70°, and 75°. The improvement becomes more pronounced as ψ increases: for example, Δ increases from −3.12 dB (uniform) to 2.55 dB (optimized) at $\psi = 60°$, and from 5.27 dB to 7.13 dB at $\psi = 75°$. These results suggest that non-uniform spacing provides limited benefit at smaller steering angles but offers a clearer advantage at moderate-to-large steering angles.

Figure 8a compares the main-lobe–sidelobe difference Δ (dB) of the uniform array and the optimized arrays (designed at ψ = 60°, 65°, 70°, and 75°) when evaluated over steering angles θ = 60–75°. The uniform array exhibits a relatively stable but generally lower Δ, indicating limited sidelobe (or grating-lobe) suppression at off-axis steering. In contrast, the optimized arrays show angle-dependent improvements, with more pronounced gains at higher steering angles ($\theta \geq 70°$), where larger Δ values indicate stronger main-lobe concentration and better sidelobe control.

Figure 8b summarizes Δ using box plots across the evaluated angles. The uniform array has a low median and a narrow interquartile range (IQR), reflecting consistent yet weaker performance. The optimized arrays generally present higher medians, demonstrating improved directivity, while exhibiting wider IQRs, suggesting increased variability associated with angle-specific optimization and the presence of multiple local optima.

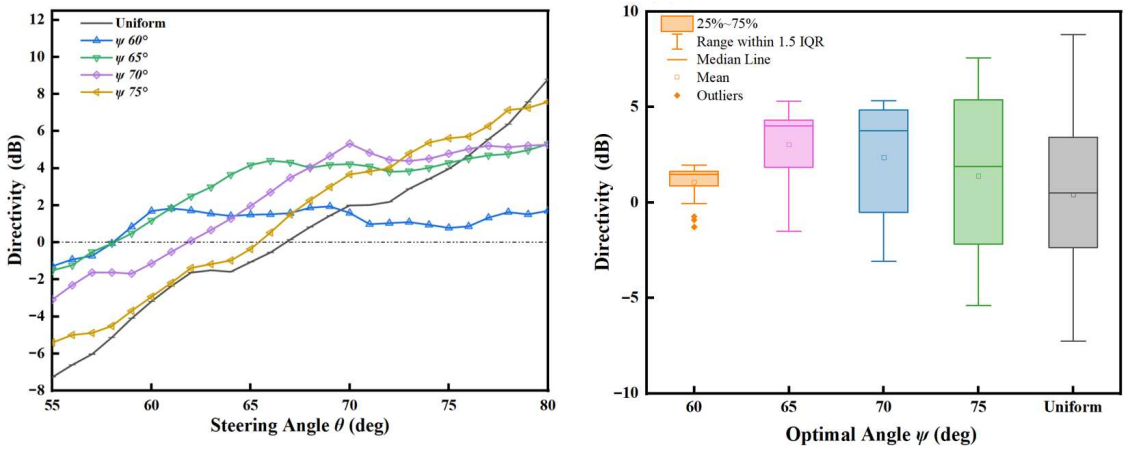

(**a**) (**b**)

Figure 8. (**a**) Comparison of the main lobe to sidelobe differences Δ (dB) for seven distinct array configurations, including a Uniform Array and six Optimized arrays, θ = 60–75°. (**b**) Box-plot summary of Δ for each configuration across all evaluated steering angles; each box depicts the interquartile range (IQR).

4.2. Westervelt Directivity Analysis

Given that the signal produced by a PAL is generated through the modulation of two high-frequency signals, nonlinear effects result in the production of a new signal at a frequency equal to the difference between the two [37]. The product directivity is calculated using the equation $D_1 * D_1$, which serves as a critical step for determining Westervelt directivity. The Westervelt directivity, as shown, follows the calculation based on function (11) referenced earlier. By combining the directivities of the two primary signals, this approach enables estimation of the nonlinear acoustic behaviour in PALs. Using this formulation, we compute the Westervelt directivity for both simulated and measured results.

From Figure 9, the optimized array exhibits a smoother directivity pattern than the uniform array. At steering angles of $\psi = 75°$, the values for the uniform array and the optimal array are quite similar. At steering angles of $\psi = 65°$ and 70°, the optimal array outperforms uniform arrays. However, at steering angles of $\psi = 60°$, the optimal array loses its high directivity, whereas both uniform arrays generate high directivity at the grating lobe angles.

Overall, The optimal array effectively reduces sidelobes at steering angles between $\psi = 65$–$75°$ while maintaining the main-lobe directivity. At lower steering angles, the benefit becomes less pronounced because prominent grating lobes are not observed for either configuration. These results indicate that the advantage of the optimized layout lies in improving sidelobe or grating-lobe control within a practical steering range.

Table 3 presents a comparative analysis of the directivity difference Δ between the main lobe and the grating lobe for both optimized and uniform arrays at $\psi = 60°$, 65°, 70°, and 75°. Both simulation and experimental results are included. The optimized arrays show higher main lobe-to-grating lobe differences, particularly at larger steering angles, confirming their superior directivity control. The comparison between simulated and experimental data further validates the effectiveness of the proposed optimization approach in real-world implementations. The optimized array exhibits a clear improvement in main grating lobe separation for $\psi = 65$–$75°$, while limited benefit is observed at $\psi = 60°$, consistent with the directivity patterns in Figure 9.

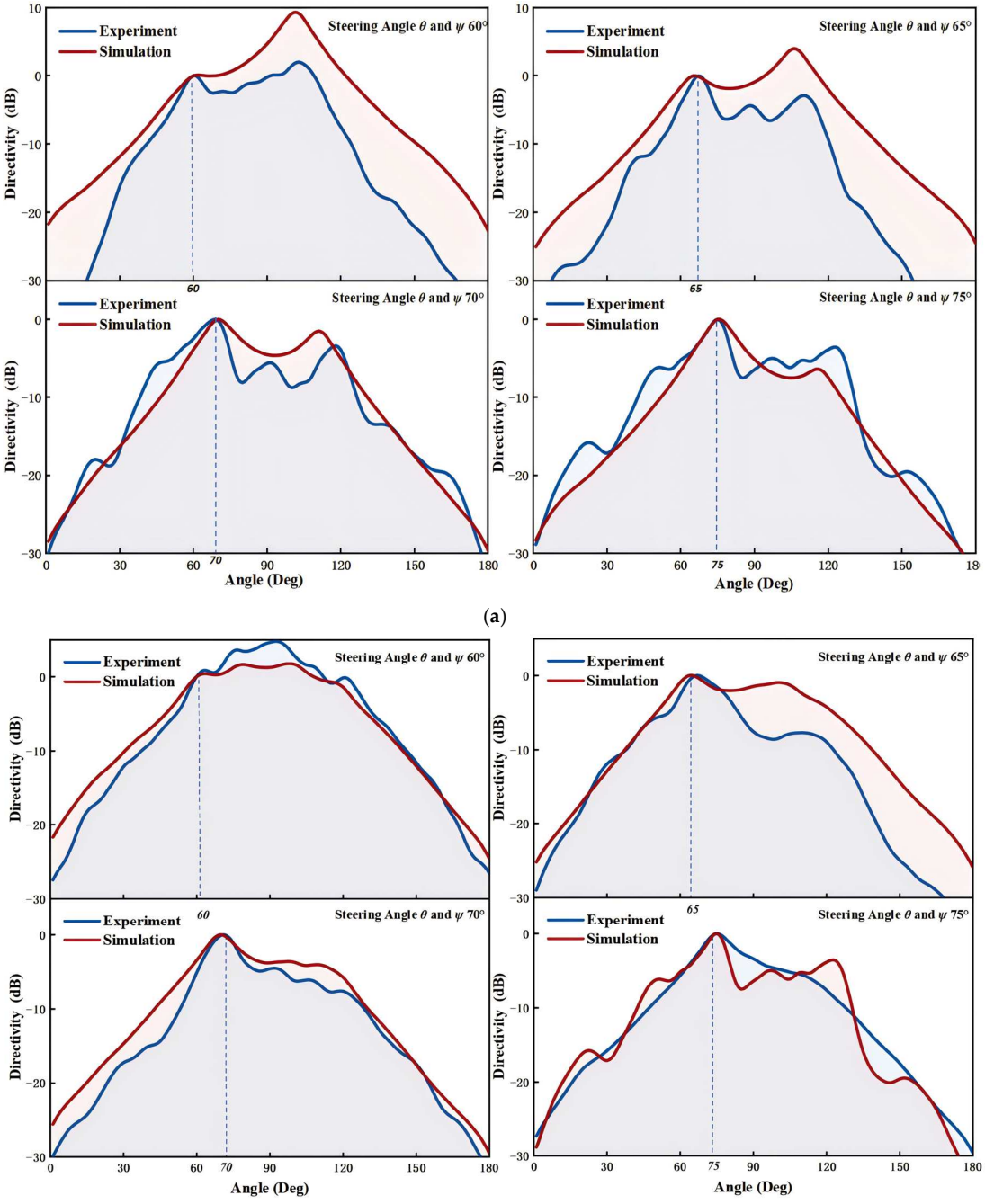

(**a**)

(**b**)

Figure 9. Simulated and measured Westervelt directivity of the uniform array (**a**) and optimal array (**b**) at 40 kHz and 42 kHz for steering angles $\psi = 60^{\circ}, 65^{\circ}, 70^{\circ}, 75^{\circ}$.

Table 3. Main grating lobe level difference at optimal steering angle ψ, defined as $\Delta = \max(L_{\text{Main}}(\psi) - L_{\text{Side}}(\psi))$. Positive values indicate effective grating-lobe suppression.

Experiment Data (dB)		
$\boldsymbol{\psi}(^{\circ})$	Uniform Array	Optimal Array
60	−1.966	−3.8191
65	2.950	5.88176
70	3.449	4.53129
75	3.538	4.47579

Table 3. *Cont.*

Simulation Data (dB)		
ψ(°)	Uniform Array	Optimal Array
60	−9.2042	−1.539
65	−4.1416	0.917
70	1.4966	3.6541
75	6.46171	5.6765

4.3. Monte Carlo Robustness Analysis

To evaluate the sensitivity and robustness of the proposed method under practical uncertainties, multiple representative cases corresponding to different steering angles were investigated through Monte Carlo analysis. The analysis explicitly accounts for element-level fabrication and driving errors while keeping the array topology and steering angle fixed for each case. For each steering angle (ψ = 60°, 65°, 70°, and 75°), both the optimized non-uniform array and the corresponding uniform array were considered, resulting in eight Monte Carlo cases in total. This design enables a fair, angle-consistent comparison between each optimized configuration and its uniform counterpart.

For each case, 100 Monte Carlo trials were performed. Position errors were modelled as independent Gaussian perturbations with a standard deviation of 0.5 mm, and amplitude errors were modelled as independent Gaussian fluctuations with a 20% standard deviation. The two error sources were sampled independently for each element and each trial. This setup reflects the practical requirement that the primary acoustic energy should remain concentrated near the intended steering direction rather than relying on the global maximum of the radiation pattern.

Figure 10 shows the Monte Carlo distributions of Δ for all eight array configurations under random element-level uncertainties. The Monte Carlo analysis is intended to verify whether the proposed numerical model can predict the performance degradation trends observed in laboratory experiments, rather than to reproduce individual experimental measurements. The red markers indicate experimental results and are shown for reference.

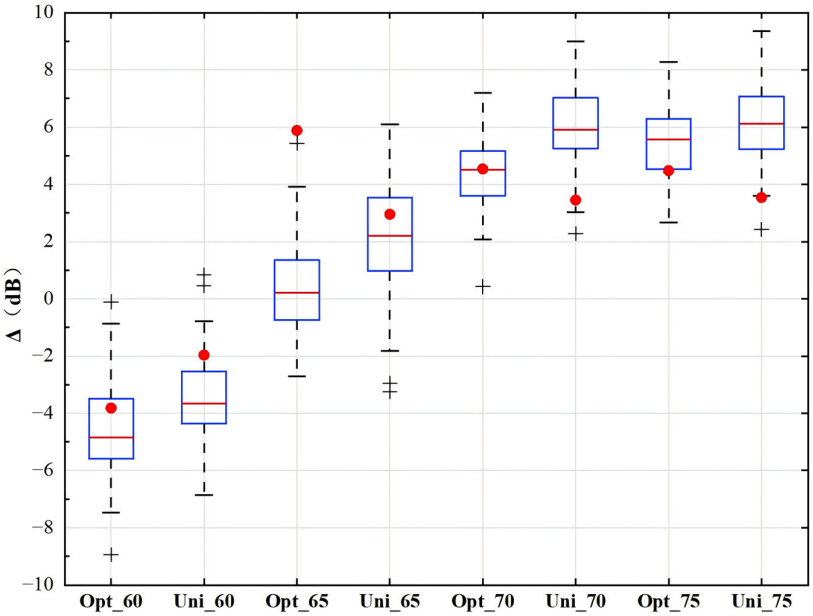

Figure 10. Monte Carlo distributions of Δ for optimized and uniform arrays at different steering angles.

Across all steering angles, the optimized arrays consistently exhibit higher mean Δ values and narrower distributions than their uniform counterparts, indicating improved robustness under combined position and amplitude uncertainties. At $\psi = 60^\circ$, both configurations show negative mean Δ values, reflecting the experimentally observed degradation under strong steering conditions, while the optimized array maintains a systematic performance advantage. As the steering angle increases, the predicted degradation becomes less pronounced, and the robustness of the optimized configurations is further enhanced.

In all cases except optimal array $\psi = 65^\circ$, the experimental measurements fall within or close to the corresponding Monte Carlo distributions, confirming that the proposed model successfully captures the experimentally observed degradation trends and provides a statistically meaningful explanation for the discrepancies between ideal simulations and laboratory results.

5. Conclusions

This study presents a systematic optimization framework for PALs aimed at improving far-field directivity under practical array constraints. By integrating a convolution-based directivity model with FEM simulations, the proposed approach enables accurate evaluation of acoustic field behaviour for non-uniform array configurations and supports efficient design iteration guided by high-fidelity numerical modelling. The framework shows consistent performance across multiple steering-angle cases and remains stable under stochastic perturbations, indicating robustness to practical uncertainties; the comparative benchmark further confirms its computational efficiency.

PSO is adopted to synthesise array layouts because it offers a favourable balance between solution quality and computational cost in high-dimensional design spaces. Both simulations and experiments show that the optimised non-uniform arrays outperform conventional uniform configurations across the tested steering range (60–75°), achieving up to a 5 dB improvement in main-lobe-to-sidelobe (or grating-lobe) separation. Simulations exhibit idealised patterns, while the measurements show the same trends with small deviations attributable to phase errors, transducer variability, and minor alignment deviations.

The results also reveal an inherent trade-off between steering capability and grating-lobe suppression, highlighting the need for application-specific design balance. Although the experimental validation was limited to a 2 m far-field measurement distance, the proposed framework offers a practical and computationally efficient route to steering-capable PAL design under non-ideal spacing conditions and provides a solid basis for future extensions such as improved hardware synchronization and uncertainty-aware optimization.

Author Contributions: Conceptualization, S.M.; methodology, S.M.; software, S.M.; validation, S.M.; formal analysis, S.M.; investigation, S.M.; resources, Y.H. and M.N.E.; data curation, S.M.; writing—original draft preparation, S.M.; writing—review and editing, Y.H. and M.N.E.; visualization, S.M.; supervision, Y.H. and M.N.E.; project administration, M.N.E.; funding acquisition, M.N.E. All authors have read and agreed to the published version of the manuscript.

Funding: This research received no external funding.

Data Availability Statement: Restrictions apply to the availability of the underlying raw measurements due to third-party facility agreements and potential intellectual property protection. Data may be shared by the corresponding author upon reasonable request and subject to appropriate confidentiality safeguards.

Acknowledgments: The authors thank the technical staff of the anechoic chamber for assistance with instrumentation and measurements.

Conflicts of Interest: The authors declare no conflicts of interest.

Abbreviations

The following abbreviations are used in this manuscript:

2D	Two-Dimensional
3D	Three-Dimensional
FEM	Finite Element Method
FE	Function Evaluation
GA	Genetic Algorithm
KZK	Khokhlov–Zabolotskaya–Kuznetsov Equation
PAL	Parametric Array Loudspeaker
PSL	Peak Sidelobe Level
PSO	Particle Swarm Optimization
QPSO	Quantum-Behaved Particle Swarm Optimization
SA	Simulated Annealing
SOS	Symbiotic Organisms Search
SPL	Sound Pressure Level
TLBO	Teaching–Learning-Based Optimization

References

1. Mei, S.; Xu, H.; Hu, Y.; Alkahtani, M.; Wang, Y. The Parametric Array Speaker: A Review. In *Proceedings of the Conference Proceedings of 2022 2nd International Joint Conference on Energy, Electrical and Power Engineering*; Hu, C., Cao, W., Eds.; Springer Nature: Singapore, 2023; pp. 1254–1271.
2. Loriga, A. Nonlinear Model and Its Inverse of an Audio System. *arXiv* **2017**, arXiv:1703.00009. [CrossRef]
3. Zhong, J.; Qiu, X. *Acoustic Waves Generated by Parametric Array Loudspeakers*; CRC Press: Boca Raton, FL, USA, 2024.
4. Zhong, J.; Kirby, R.; Qiu, X. A Spherical Expansion for Audio Sounds Generated by a Circular Parametric Array Loudspeaker. *J. Acoust. Soc. Am.* **2020**, *147*, 3502–3510. [CrossRef] [PubMed]
5. Kumar, M.J.; Praveen, P.; Dheeraj, N.; Kumar, K. Heavy Hypersonic Dual Acoustic System. *Dept. Electron. Commun. Eng., Anil Neerukonda Inst. Technol. Sci.(ANITS), Sangivalasa, Bheemunipatnam Mandal, Visakhapatnam, India, B. Tech. Project Rep* **2021**. Available online: https://nriims.info/ece/Project%20Reports%202020-21%20NAAC/Sec-C/C-16.pdf (accessed on 12 January 2026).
6. Zhong, J.; Kirby, R.; Karimi, M.; Zou, H. A Cylindrical Expansion of the Audio Sound for a Steerable Parametric Array Loudspeaker. *J. Acoust. Soc. Am.* **2021**, *150*, 3797–3806. [CrossRef]
7. Olszewski, D.; Linhard, K. 3g-3 Optimum Array Configuration for Parametric Ultrasound Loudspeakers Using Standard Emitters. In Proceedings of the 2006 IEEE Ultrasonics Symposium, Vancouver, BC, Canada, 3–6 October 2006; IEEE: New York, NY, USA, 2006.
8. Tanaka, N.; Tanaka, M. Active Noise Control Using a Steerable Parametric Array Loudspeaker. *J. Acoust. Soc. Am.* **2010**, *127*, 3526–3537. [CrossRef] [PubMed]
9. Adachi, A.; Hashiguchi, H. Application of Parametric Speakers to Radio Acoustic Sounding System. *Atmos. Meas. Tech.* **2019**, *12*, 5699–5715. [CrossRef]
10. Nakagawa, K.; Shi, C.; Kajikawa, Y. Beam Steering of Portable Parametric Array Loudspeaker. In Proceedings of the 2019 Asia-Pacific Signal and Information Processing Association Annual Summit and Conference (APSIPA ASC), Lanzhou, China, 18–21 November 2019; IEEE: New York, NY, USA, 2019; pp. 1824–1827.
11. Komatsuzaki, T.; Iwata, Y. Active Noise Control Using High-Directional Parametric Loudspeaker. *J. Environ. Eng.* **2011**, *6*, 140–149. [CrossRef]
12. Tanaka, K.; Shi, C.; Kajikawa, Y. Binaural Active Noise Control Using Parametric Array Loudspeakers. *Appl. Acoust.* **2017**, *116*, 170–176. [CrossRef]
13. Tang, K.; Wang, Y.; Wang, S.; Gao, D.; Li, H.; Liang, X.; Sebbah, P.; Li, Y.; Zhang, J.; Shi, J. Hyperuniform Disordered Parametric Loudspeaker Array. *Phys. Rev. Appl.* **2023**, *19*, 054035. [CrossRef]
14. Zhong, J.; Zou, H.; Lu, J.; Zhang, D. A Modified Convolution Model for Calculating the Far Field Directivity of a Parametric Array Loudspeaker. *J. Acoust. Soc. Am.* **2023**, *153*, 1439–1451. [CrossRef]
15. Fan, F.; Zhu, Y.; Ma, W.; Qin, L.; Wu, M.; Kuang, Z.; Yang, J. A Least Squares Based Optimization Method for Grating Lobes Suppression in Parametric Array Loudspeakers. *Appl. Acoust.* **2025**, *237*, 110757. [CrossRef]
16. Ballad, E.M.; Vezirov, S.Y.; Pfleiderer, K.; Solodov, I.Y.; Busse, G. Nonlinear Modulation Technique for NDE with Air-Coupled Ultrasound. *Ultrasonics* **2004**, *42*, 1031–1036. [CrossRef] [PubMed]

17. Ji, P.; Gan, W.-S.; Tan, E.-L.; Yang, J. Performance Analysis on Recursive Single-Sideband Amplitude Modulation for Parametric Loudspeakers. In Proceedings of the 2010 IEEE International Conference on Multimedia and Expo, Singapore, 19–23 July 2010; IEEE: New York, NY, USA, 2010; pp. 748–753.
18. Ji, P.; Ye, C.; Tian, J. Development of a Directional Loudspeaker System for Sound Reproduction. In Proceedings of the 2007 IEEE International Conference on Multimedia and Expo, Beijing, China, 2–5 July 2007; IEEE: New York, NY, USA, 2007; pp. 591–594.
19. Mu, Y.; Ji, P.; Ji, W.; Wu, M.; Yang, J. Modeling and Compensation for the Distortion of Parametric Loudspeakers Using a One-Dimension Volterra Filter. *IEEE/ACM Trans. Audio Speech Lang. Process.* **2014**, *22*, 2169–2181.
20. Saunders, G.A. Physical Ultrasonics. *Phys. Bull.* **1970**, *21*, 364. [CrossRef]
21. Gan, W.-S.; Yang, J.; Kamakura, T. A Review of Parametric Acoustic Array in Air. *Appl. Acoust.* **2012**, *73*, 1211–1219. [CrossRef]
22. Jamunaa, D.; Mahanti, G.K.; Hasoon, F.N. Synthesis of Phase-Only Position Optimized Reconfigurable Uniformly Excited Linear Antenna Arrays with a Single Null Placement. *J. King Saud Univ. Eng. Sci.* **2020**, *32*, 360–367. [CrossRef]
23. Cervenka, M.; Bednarik, M. Non-Paraxial Model for a Parametric Acoustic Array. *J. Acoust. Soc. Am.* **2013**, *134*, 933–938. [CrossRef]
24. Shi, C.; Kajikawa, Y. A Convolution Model for Computing the Far-Field Directivity of a Parametric Loudspeaker Array. *J. Acoust. Soc. Am.* **2015**, *137*, 777–784. [CrossRef]
25. Blackstock, D.T. *Fundamentals of Physical Acoustics*; John Wiley & Sons: Hoboken, NJ, USA, 2000.
26. Poli, R. Analysis of the Publications on the Applications of Particle Swarm Optimisation. *J. Artif. Evol. Appl.* **2008**, *2008*, 685175. [CrossRef]
27. Shi, Y. Particle Swarm Optimization: Developments, Applications and Resources. In Proceedings of the 2001 Congress on Evolutionary Computation (IEEE Cat. No. 01TH8546), Seoul, Republic of Korea, 27–30 May 2001; IEEE: New York, NY, USA, 2001; Volume 1, pp. 81–86.
28. Černý, V. Thermodynamical Approach to the Traveling Salesman Problem: An Efficient Simulation Algorithm. *J. Optim. Theory Appl.* **1985**, *45*, 41–51. [CrossRef]
29. Ingber, L. Simulated Annealing: Practice versus Theory. *Math. Comput. Model.* **1993**, *18*, 29–57. [CrossRef]
30. Henderson, D.; Jacobson, S.H.; Johnson, A.W. The Theory and Practice of Simulated Annealing. In *Handbook of Metaheuristics*; Glover, F., Kochenberger, G.A., Eds.; International Series in Operations Research & Management Science; Kluwer Academic Publishers: Boston, MA, USA, 2003; Volume 57, pp. 287–319, ISBN 978-1-4020-7263-5.
31. Kazemian, A.; Wang, P.; Zhuang, Y.; Yi, Y. Optimization of the Silicon-Based Aperiodic Optical Phased Array Antenna. *Opt. Lett.* **2021**, *46*, 801–804. [CrossRef] [PubMed]
32. Wang, Y.; Xu, H.; Wang, B.; Sun, M. Optimal Array Phase Center Study for Frequency-Domain Constrained Space-Time Broadband Beamforming. *IEEE Access* **2023**, *11*, 1295–1305. [CrossRef]
33. Zhang, Z.; Su, J. A Novel Optimization Approach for Phased Array Beamforming. In Proceedings of the 2020 7th International Conference on Information Science and Control Engineering (ICISCE), Changsha, China, 18–20 December 2020; IEEE: New York, NY, USA, 2020; pp. 2295–2297.
34. Dufossé, P.; Enderli, C.; Savy, L.; Hansen, N. Phased-Array Antenna Pattern Optimization with Evolution Strategies. In Proceedings of the 2020 IEEE Radar Conference (radarconf20), Florence, Italy, 21–25 September 2020; IEEE: New York, NY, USA, 2020; pp. 1–6.
35. Lee, K.C.-M.; Gan, W.-S. Bandwidth-Efficient Recursive Pth-Order Equalization for Correcting Baseband Distortion in Parametric Loudspeakers. *IEEE Trans. Audio Speech Lang. Process.* **2006**, *14*, 706–710.
36. Shapiro, J. Genetic Algorithms in Machine Learning. In *Machine Learning and Its Applications*; Paliouras, G., Karkaletsis, V., Spyropoulos, C.D., Eds.; Lecture Notes in Computer Science; Springer: Berlin/Heidelberg, Germany, 2001; Volume 2049, pp. 146–168, ISBN 978-3-540-42490-1.
37. Mei, S.; Hu, Y.; Alkahtani, M.; Esfahani, M.N. A Dual Convolution Model for Grating Lobe Prediction in Directivity of Parametric Array Loudspeakers. *IEEE Access* **2025**, *13*, 39183–39191. [CrossRef]